

# Efficient Radiation Treatment Planning based on Voxel Importance

Sebastian Mair<sup>1</sup>, Anqi Fu<sup>2</sup> and Jens Sjölund<sup>1</sup>

<sup>1</sup> Uppsala University, Sweden

<sup>2</sup> Memorial Sloan-Kettering Cancer Center, New York, USA

E-mail: [sebastian.mair@it.uu.se](mailto:sebastian.mair@it.uu.se), [fua@mskcc.org](mailto:fua@mskcc.org), [jens.sjolund@it.uu.se](mailto:jens.sjolund@it.uu.se)

**Abstract.** *Objective.* Optimization is a time-consuming part of radiation treatment planning. We propose to reduce the optimization problem by only using a representative subset of informative voxels. This way, we improve planning efficiency while maintaining or enhancing the plan quality.

*Approach.* To reduce the computational complexity of the optimization problem, we propose to subsample the set of voxels via importance sampling. We derive a sampling distribution based on an importance score that we obtain from pre-solving an easy optimization problem involving a simplified probing objective. By solving a reduced version of the original optimization problem using this subset, we effectively reduce the problem's size and computational demands while accounting for regions in which satisfactory dose deliveries are challenging.

*Main results.* In contrast to other stochastic (sub-)sampling methods, our technique only requires a single sampling step to define a reduced optimization problem. This problem can be efficiently solved using established solvers. Empirical experiments on open benchmark data highlight substantially reduced optimization times, up to 50 times faster than the original ones, for intensity-modulated radiation therapy (IMRT), all while upholding plan quality comparable to traditional methods.

*Significance.* Our approach has the potential to significantly accelerate radiation treatment planning by addressing its inherent computational challenges. We reduce the treatment planning time by reducing the size of the optimization problem rather than improving the optimization method. Our efforts are thus complementary to much of the previous developments.

*Keywords:* radiation treatment planning, importance sampling, subsampling, optimization

## 1. Introduction

Radiation treatment planning (RTP) is widely used for cancer treatment, where the goal is to achieve tumor control by delivering a sufficiently high dose to the target while sparing healthy tissue to the maximum possible extent. This is often formulated as a constrained optimization problem where potentially conflicting objectives, such as tumor control and normal tissue sparing, are combined as a weighted sum in the objective function. The constraints are usually dictated by the physics and the hardware but can also include clinical considerations such as the maximum dose in an organ at risk. Since the problem is often high-dimensional, both in terms of decision variables and constraints, it can be computationally demanding to solve. What makes matters worse, however, is that the weights of the different objective terms are difficult to determine a priori and, therefore, requires a human (clinician) in the loop (Miettinen; 1999; Romeijn et al.; 2004). Consequently, many manual iterations are often needed to find a satisfactory trade-off. This has motivated the wealth of research on efficient optimization methods tailored to RTP. We, too, share the aim of reducing the planning time in RTP, but rather than improving the optimization *solver*, we focus on reducing the size of the optimization *problem*. Our efforts are thus complementary to much of the previous developments.

Standard formulations of the optimization problem consider all voxels in the regions of interest as if the voxel doses could be controlled independently by optimizing the beamlet intensities. On the contrary, it follows from elementary radiation physics that the absorbed dose is strongly correlated in space due to effects such as Compton scattering and pair production (Fippel; 1999). A key insight behind our approach is that a cleverly chosen subset of the voxels effectively pins down the dose absorbed in other areas of relevance. Such a subsampled optimization problem can be solved much faster than the full one. This immediately raises two questions. First, how can we identify such a representative subset? Second, can it be done efficiently enough to reduce the overall solution time?

In this paper, we describe an approach that answers these questions affirmatively. Specifically, we derive an importance sampling strategy that automatically identifies a representative subset of voxels by *probing*, *i.e.*, approximately solving a simplified version of the optimization problem at hand. Our results demonstrate that we can reduce the solution time of IMRT problems to less than 7%, 1.6%, and 47% for *prostate*, *liver*, and *head and neck* cases, respectively, with essentially no difference in plan quality.

In contrast to the stochastic optimization method of Martin et al. (2007), we sample just *once* to define an optimization problem with substantially fewer constraints, which can then be solved with the solver of choice (according to the rich literature on RTP, see, *e.g.*, Wächter and Biegler (2006); Aleman et al. (2010); Unkelbach et al. (2015); O'Donoghue et al. (2016); Stellato et al. (2020)). This is similar to Thieke et al. (2002) and Sjölund et al. (2019), both of which used a geometric approach to define a representative subset. In contrast, our approach is entirely data-driven and thereby

accounts for case-specific differences, paving the way for personalized medicine.

We believe that probing, owing to its simplicity and efficiency, presents an appealing approach to shorten treatment planning times.

## 2. Method

### 2.1. Notation and problem setting

Consider a patient volume consisting of  $n \in \mathbb{N}$  voxels and let  $n_b \in \mathbb{N}$  be the number of beamlets. Given a beam configuration, we can simulate the dose each body voxel receives using an appropriate dose calculation technique (Ahnesjö and Aspradakis; 1999). We focus on fluence map optimization, where the goal is to find the beamlet intensities  $x \in \mathbb{R}_{\geq 0}^{n_b}$  yielding specific voxel doses  $y \in \mathbb{R}_{\geq 0}^n$  that satisfy some clinical objectives. The relationship between beamlet intensities and voxel doses is approximately linear, and described by a dose influence matrix  $A \in \mathbb{R}_{\geq 0}^{n \times n_b}$  such that  $Ax = y$ . The non-negativity of  $A$  and  $x$  are due to physical constraints and naturally yield a non-negative dose vector  $y$ . We associate each voxel with a target dose  $t \in \mathbb{R}_{\geq 0}^n$  that is prescribed on a voxel basis. The set of voxels  $\mathcal{V} = [n] \stackrel{\text{def}}{=} \{1, 2, \dots, n\}$  is commonly divided into a group of distinct non-overlapping structures representing the planning target volume (PTV), organs at risk (OARs), and other generic body parts (BDY). The resulting optimization problem is of the form

$$\min_{x,y} f(y) \quad \text{s.t.} \quad Ax = y, \quad y \in \mathcal{C}, \quad x \geq 0, \quad (1)$$

where  $\mathcal{C}$  denote some (usually affine) constraints, *e.g.*, mean and max dose constraints. The dose penalty function  $f$  is usually convex and separable in the number of voxels, *i.e.*,

$$f(y) = \sum_{s \in \mathcal{S}} \sum_{v \in \mathcal{V}_s} \frac{1}{|\mathcal{V}_s|} f_s(y_v). \quad (2)$$

Here,  $s \in \mathcal{S}$  denotes a structure,  $\mathcal{S} = \{\text{PTV}, \text{OAR}, \text{BDY}\}$  is the set of all structures,  $v \in [n]$  is the index of a voxel, and  $\mathcal{V}_s$  is the set of all voxels in structure  $s$ . The per-voxel penalty is often of a form such as (Romeijn et al.; 2003; Fu et al.; 2019; Sjölund et al.; 2019)

$$f_s(y_v) = \frac{1}{\max(t_s, \tau_s)^p} \left( \underbrace{w_s^- \cdot ([y_v - t_v]^-)^p}_{\text{underdosing}} + \underbrace{w_s^+ \cdot ([y_v - t_v]^+)^p}_{\text{overdosing}} \right), \quad (3)$$

where  $p \in \{1, 2\}$  is an exponent,  $t_v$  denotes the target dose per voxel,  $t_s$  indexes the vector of target doses per structure,  $\tau_s > 0$  is a threshold that prevents a division by zero,  $y_v$  is the dose per voxel, and  $w_s^-, w_s^+ \geq 0$  are structure-dependent weights that penalize underdosing and overdosing, respectively. Here, we use the element-wise operators  $[z]^- = \max(-z, 0)$  and  $[z]^+ = \max(z, 0)$ . Note that the leading division in Equation (3) normalizes the penalty by the corresponding target dose  $t_s$ , in addition to the normalization by the number of voxels per structure  $|\mathcal{V}_s|$  in Equation (2). Therefore, we can expect that the contribution of each structure to the objective function value is on the

order of one.<sup>‡</sup> Often, organs at risk have a target dose of zero. Thus, setting a threshold, *e.g.*,  $\tau_{\text{OAR}} = 1$  prevents a division by zero. If  $\mathcal{C}$  is an affine set, then choosing  $p = 1$  within the per-voxel penalty  $f_s$  in Equation (3) yields a resulting optimization problem in Equation (1) that is a linear program (LP) while  $p = 2$  yields a quadratic program (QP).

Since the per-voxel penalty in Equation (3) is a convex function, so is the problem in Equation (1) as a whole, as long as  $\mathcal{C}$  is convex. Nevertheless, it is non-trivial to optimize because of the large scale and the (nominal) non-smoothness of the per-voxel penalty. Moreover, the individual weights  $w_s^-$  and  $w_s^+$  have to be chosen per structure  $s$ , which results in another optimization problem.

## 2.2. Efficiency through subsampling

We propose to restrict the computation of the treatment plan and, thus, the costly optimization problem to only use a *representative subset* of voxels. Thus, instead of using all  $n$  voxels, we only use  $m \ll n$  *informative* voxels. The computational savings in time are then amplified when a selection of the structure-dependent penalty weights  $w_s^-$  and  $w_s^+$  is performed.

The idea is as follows. We first optimize a simple probing function that approximates the original problem from Equation (1) but is much easier to optimize (Subsection 2.3). Based on the probing function, we derive a *per-voxel score* that is indicative of a voxel’s informativeness (Subsection 2.4). Specifically, we expect that non-target voxels close to the PTV and non-target voxels directly intersected/traversed by the beam are important. We then turn the scores into a probability distribution over voxels and sample a subset of voxels (Subsection 2.5). After eliminating voxels anticipated to have low impact via subsampling, we can solve all remaining optimization problems (Equation (1)) faster and more efficiently using this smaller data set.

## 2.3. Probing function

Consider a simplified per-voxel penalty that does not have any additional parameters and neither distinguishes between structures nor overdosing and underdosing, *i.e.*,  $f_s(y_v) = (y_v - t_v)^2$ , where  $y_v = A_{v,:}x$ . Plugging this simplified per-voxel penalty into the optimization problem in Equation (1) and neglecting the dose constraints  $y \in \mathcal{C}$  results in the simple non-negative least squares problem:

$$\min_{x \geq 0} f_{\text{probing}}(x), \quad \text{where} \quad f_{\text{probing}}(x) = \sum_{s \in \mathcal{S}} \sum_{v \in \mathcal{V}_s} \frac{1}{|\mathcal{V}_s|} (A_{v,:}x - t_v)^2. \quad (4)$$

We optimize this simplified objective over *all* voxels using  $x_0 = 0$  as an initial point. This initialization is reasonable since it yields a dose of zero for all voxels, which is already ideal for all non-PTV voxels. The optimization procedure now has to adapt the configuration  $x$  to reach the target dose on PTV voxels while keeping the doses of OAR and BDY voxels low. We utilize projected gradient descent (PGD)<sup>§</sup>, where the

<sup>‡</sup> As a physicist might say, the objective function is non-dimensionalized.

<sup>§</sup> Note that a closed-form solution is impossible due to the non-negativity constraints.

projection onto the non-negative orthant can be made by simply clipping the negative coordinates in  $x$  to zero. After only a few iterations of the form

$$x_{k+1} = \left[ x_k - \eta \frac{d}{dx} f_{\text{probing}}(x_k) \right]^+,$$

where  $\eta > 0$  is a step-size, we should be able to quantify which voxels are important, *i.e.*, by their contribution to the objective.

#### 2.4. Scoring voxels based on their importance

To derive importance scores, we adopt an approach from Paul et al. (2021) to our scenario. The idea is as follows. We start by optimizing a cheap surrogate optimization problem, *i.e.*, the probing function in Equation (4). Let  $g_k(v) = \frac{d}{dx} \frac{1}{|V_s|} f_s(y_v)$ , where  $y_v = A_{v,:}x$ , denote the gradient of the probing function of voxel  $v$  at iteration  $k$  of projected gradient descent. Paul et al. (2021) show that the influence of a voxel  $v$  given the current beam intensities  $x_k$  during optimization depends on its gradient norm, *i.e.*,  $\|g_k(v)\|$ . Phrased differently, voxels with a small gradient norm have a small influence on the overall per-voxel penalty. Likewise, we expect a high influence of voxels that have a large gradient norm. From an optimization point of view, any voxel that receives a dose different from its target dose does not only contribute positively to the objective function value but also yields a gradient with a positive norm. Hence, the gradient norm serves as a measure of importance.

In summary, we define the importance score as  $\chi_k(v) = \|g_k(v)\|$ , which depends on the number of steps  $k$  of PGD. In practice, we only derive this score after optimizing the probing function in Equation 4. For completeness, we provide the derivation of the score in Appendix A.

#### 2.5. Subsampling voxels

We now derive a sampling strategy based on importance sampling and start by turning the scores into a sampling distribution  $q$  by normalizing the importance scores, *i.e.*,  $q(v) = \frac{\chi(v)}{\sum_{v'} \chi(v')}$ . Using the sampling distribution  $q$ , we can now sample a subset  $\mathcal{S} \subset \mathcal{V}$  of size  $m \ll n$  and re-weight the per-voxel penalty in Equation (3) for every chosen voxel by multiplying by  $\frac{1}{m \cdot q(v)}$ . This re-weighting of voxels is needed so that the – now reduced – objective function yields an unbiased estimate of the objective function on all voxels. To ease notation, let us first define  $\mathcal{L}(\mathcal{V}) \stackrel{\text{def}}{=} f(y)$  and  $\tilde{f}(y_v) \stackrel{\text{def}}{=} \frac{1}{|V_s|} f_s(y_v)$ , where  $s$  is the structure the voxel  $v$  belongs to. Thus,  $\mathcal{L}(\mathcal{V}) = \sum_{v \in \mathcal{V}} \tilde{f}(y_v)$  is the sum of penalties over all voxels  $\mathcal{V}$  and let  $\mathcal{L}(\mathcal{S}) = \sum_{v \in \mathcal{S}} \frac{1}{m \cdot q(v)} \tilde{f}(y_v)$  be the sum of re-weighted penalties over all subsampled voxels  $\mathcal{S}$ .

An example of a sampling distribution and corresponding samples is shown in Figure 1 for a prostate case. Note that BDY voxels are primarily sampled from the five radiation corridors. Apart from BDY voxels, boundary areas between PTV and OAR are sampled more often. The highest density is assigned to the boundary of the PTV.

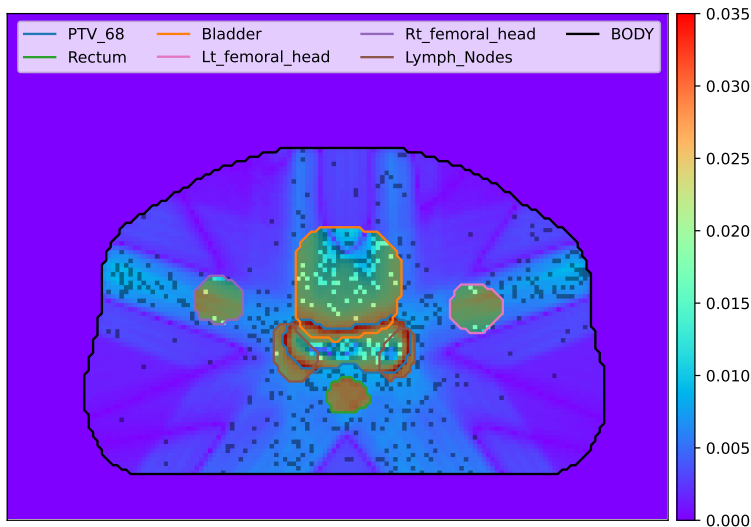


Figure 1: Sampling distribution  $q(v)$  for a prostate case including  $m = 51,778$  sampled voxels corresponding to 7.5% of voxels.

### 3. Results

#### 3.1. Data

In our experiments, we use the CORT data set (Craft et al.; 2014), which comes with four cases. Neglecting the phantom case, we evaluate our proposed approach on a *prostate*, *liver*, and *head and neck* case. For all cases, we fix the couch angle to zero degrees, and we use five equally spaced gantry angles, *i.e.*, 0, 72, 144, 216, and 288 degrees, for the prostate case. For the liver case, we use six gantry angles, *i.e.*, 32, 90, 148, 212, 270, and 328, and for the head and neck case, we use seven gantry angles, *i.e.*, 0, 52, 104, 156, 208, 260, and 312. More information on the data is provided in Table 1.

Table 1: Case specific information and settings

Information/Setting	Prostate	Liver	Head and Neck
Number of PTV voxels	6,770	6,954	5,768
Number of OAR voxels	26,469	148,318	2,162
Number of BDY voxels	657,134	1,772,085	243,963
Number of beamlets $n_b$	721	389	7,906
$t_{PTV}$	68 Gy	56 Gy	70 Gy
$t_{OAR}$ and $t_{BDY}$	0 Gy	0 Gy	0 Gy
All $\tau_s$	5 Gy	5 Gy	5 Gy
Chosen OAR structures	bladder, left and right femoral heads, lymph nodes, penile bulb, and rectum	heart, liver, spinal cord, and stomach	brain stem, chiasma, larynx, lips, left and right parotid, and spinal cord
Body structure	body	skin	external

### 3.2. Setup

All experiments run on an Intel Xeon machine with 28 cores with 2.60 GHz and 256 GB of memory and are implemented in Python using `numpy` (Harris et al.; 2020) and `CVXPY` Diamond and Boyd (2016). We compare our proposed subsampling approach (`gradnorm`) against uniform subsampling (`uniform`), *i.e.*, using  $\chi(v) = c$ , where  $c > 0$  is an arbitrary constant, and the full solution (`full`), *i.e.*, solving the optimization problem in Equation (1) on all data. For the solver, we use `MOSEK`. When optimizing the problem in Equation (1), we set the target doses for the OAR and BDY structures equal to  $t_s = 5$  Gy. This way, we penalize overdosing only for voxels that exceed a dose of  $t_s$ . For the probing function, we run projected gradient descent on Equation (4) for 20 iterations from an initial configuration  $x_0 = 0$  with a step size of  $\eta = 2(\sigma_{\min}(2A^T A) + \sigma_{\max}(2A^T A))^{-1}$ . Due to the stochasticity of the subsampling approaches, we repeat each experiment 50 times with different seeds and report on median performances. In addition, we depict the 75% and 25% quartiles. We use subsample sizes  $m$  between 0.25% and 90% of the total number of voxels per case. Unless stated otherwise, we present results for the choice of  $p = 2$ , *i.e.*, quadratic programming. The weights  $w_s^\pm$  were chosen such that `full` yields an acceptable dose-volume histogram (DVH). Settings specific to the cases are described in Table 1.

### 3.3. Evaluating subsampling approaches using dose-volume histograms

We now consider the prostate case, evaluate different subsampling sizes for `gradnorm`, and compare the performance in terms of DVHs against `uniform` and `full`. Figure 3 (left) depicts the DVH of `full` (solid lines) and the optimization of Equation (4) using projected gradient descent (PGD) after  $k = 20$  steps (dashed lines). The solution  $x_{20}$  after 20 PGD steps yields a sub-optimal yet already informative solution and is used to derive the importance scores. The resulting sampling distribution for a specific slice is depicted in Figure 1.

After subsampling voxels according to the `gradnorm` and `uniform` strategies, and thus reducing the size of the optimization problem in Equation (1), we can evaluate their performances. Figure 2 depicts the results for `gradnorm` and `uniform` on the left and right columns, respectively. Furthermore, the rows show various interesting subsampling sizes. In all subplots, the medians of the subsampling approaches are depicted as dashed lines, while `full` is shown as solid lines. The shaded areas reflect the 75% and 25% quartiles of all 50 repetitions.

We can see that `gradnorm` already approximates the PTV very well by using only 0.25% of the voxels, while `uniform` needs more than 20% to achieve a similar approximation. Besides, almost all OARs are sufficiently well approximated using `gradnorm` with only 7.5% of all voxels. Note that the larger the subsample size  $m$ , the smaller the uncertainty. The results for the liver and head and neck cases are

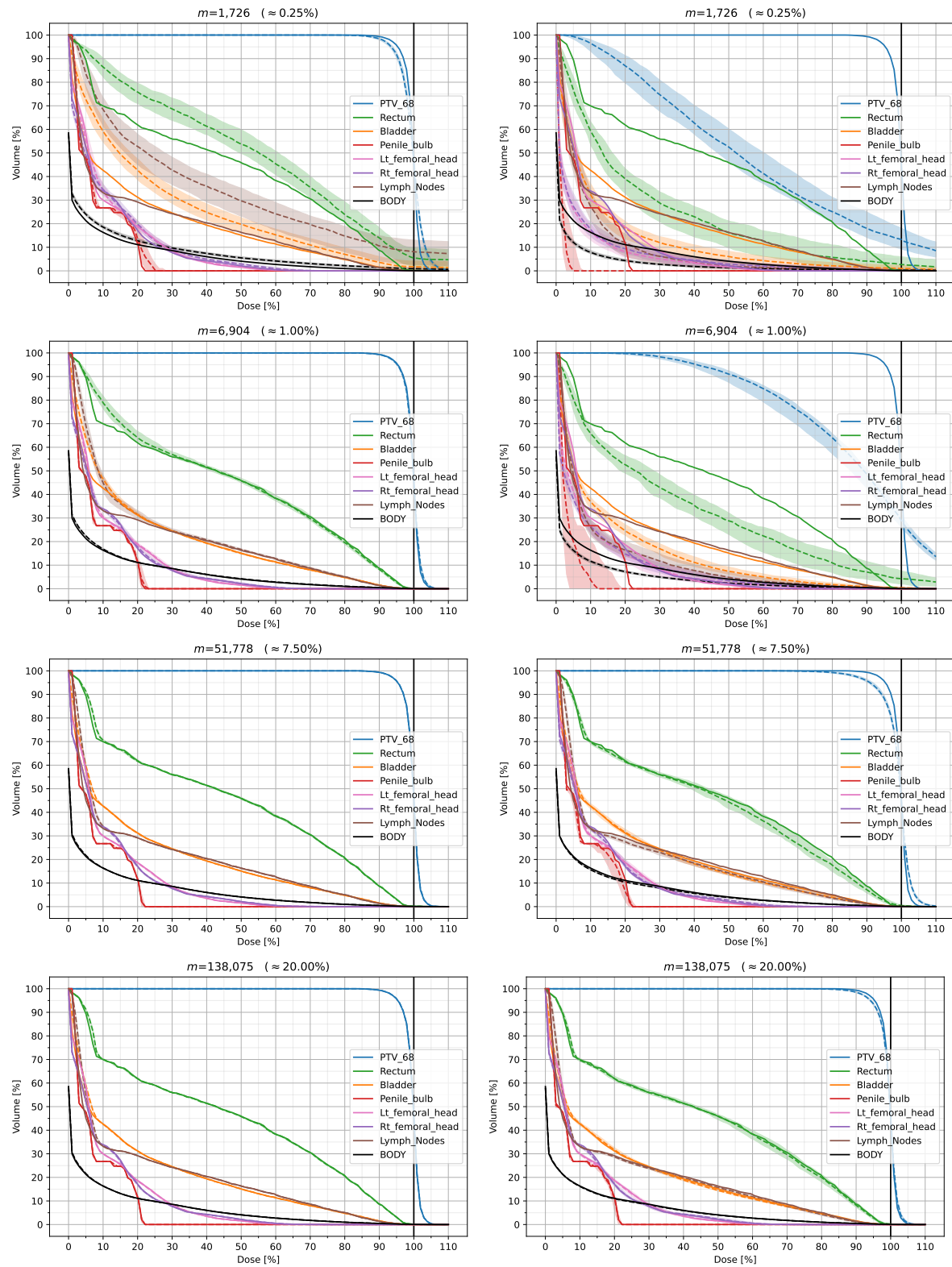


Figure 2: Dose-volume histograms for the prostate case and  $p = 2$ . Solid lines are the DVH from solving the problem with the full data set. The left column depicts the results of our proposed **gradnorm** subsampling approach while the right column shows **uniform** subsampling. The rows depict different subsampling sizes  $m$  and the percentage of  $m$  relative to the total number of voxels  $n$ .



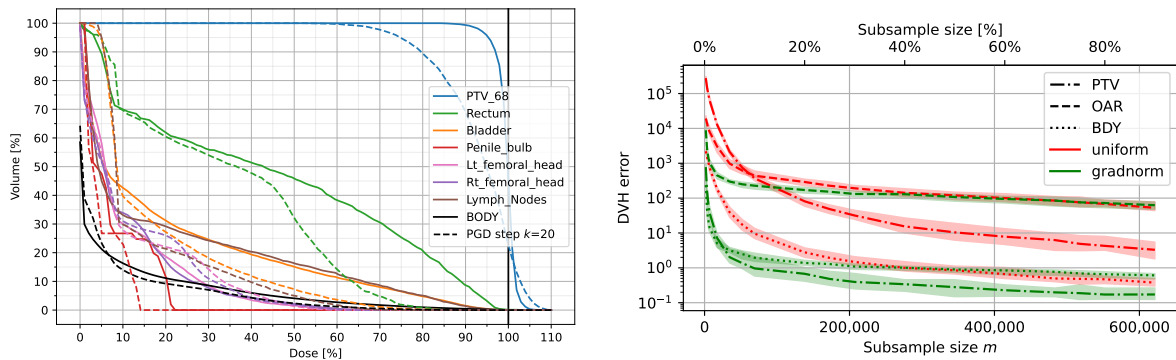


Figure 3: Left: Dose-volume histograms for the prostate case of **full** (solid lines) and the projected gradient descent (PGD) optimization after  $k = 20$  steps (dashed lines) which we use as a probing function to derive the importance scores. Right: Error of dose-volume histogram approximations of **uniform** and **gradnorm** when compared to **full** for the prostate case. The error is split among the structures  $S = \{PTV, OAR, BDY\}$ .

deferred to Appendix B.

In Figure 3 (right), we aggregate the results shown in Figure 2. Here, we compute the DVH error as a squared error between the DVH lines of the subsample approaches and **full** at 111 positions (from 0% to 110%). As seen in the figure, regardless of the subsample size, **gradnorm** yields lower errors than **uniform** for all structures.

### 3.4. Evaluating subsampling approaches using the objective function

Next, we evaluate the relative objective function value. That is, the objective function value of the solution obtained from the reduced problem is divided by the objective function value of the solution obtained from the full problem. The results are depicted in Figure 4 (left). Once again, our **gradnorm** yields very quickly much better approximations than **uniform**. Note that using 7.5% of the data yields an objective function value that deviates less than 1% of the corresponding one from the full problem.

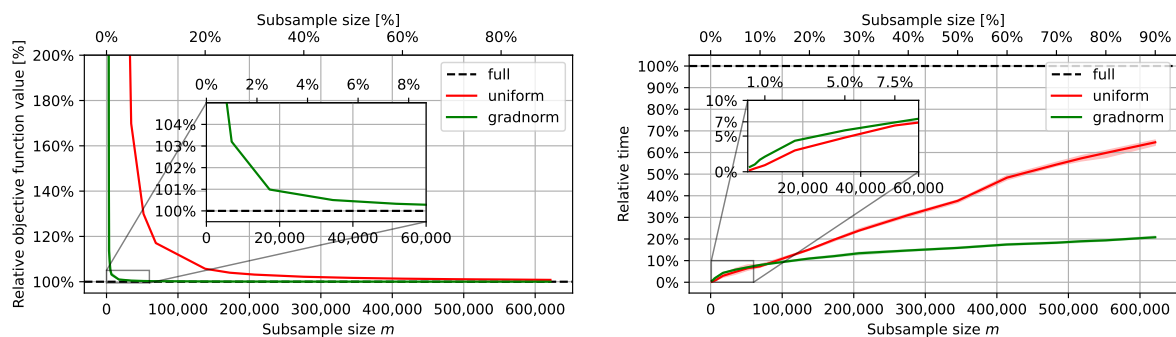


Figure 4: Relative objective function values (left) and computation time (right) of **uniform** and **gradnorm** when compared to **full** for the prostate case.

### 3.5. Evaluating subsampling approaches in terms of computational time

Finally, we evaluate the time it takes to compute the radiation plans on the reduced optimization problems. Figure 4 (right) depicts the relative computation times of `uniform` and `gradnorm` when compared to `full` for all three cases. Note that `gradnorm` reduces the computation time to only approximately 20% of the original time, regardless of the subsample size. Specifically, using only 7.5% of all voxels for `gradnorm` reduces the computation time to less than 7%.

## 4. Discussion

When it comes to comparing the proposed subsampling strategy from Subsection 2.5 to uniform subsampling, we can see from Figure 1 that our approach indeed leverages information, *e.g.*, about the beam directions, obtained from the probing function. Thus, our strategy can be seen as being *data-driven*. On the contrary, the uniform subsampling strategy does not have such additional information, and the user would need to adapt the strategy to include this information. Note that in our proposed subsampling strategy, important voxels are sampled more often and are assigned a lower weight. In contrast, less important voxels get sampled less often but are assigned a higher weight.

Since our strategy focuses on important or informative regions, it happens that we sample the same voxel multiple times. Thus, the same penalty term appears multiple times in Equation (2), which potentially leads to problems during optimization. However, we can simply aggregate those terms by summing their weights. A positive side-effect of this strategy is that the computation time does not necessarily increase at the same rate as the subsample size, see Figure 4 (right).

Earlier, we made the point that the underdosing and overdosing penalty weights  $w_s^\pm$  per structure  $s$  have to be optimized as well, resulting in a bilevel optimization task. This further amplifies our time savings per optimization run.

Although our approach is inspired by Paul et al. (2021), it differs in several aspects. First, Paul et al. (2021) consider a neural network-based classifier while we use a (weighted) non-negative linear regression. Second, they take the  $m$  points with the largest scores while we turn the scores into a sampling distribution and subsample the set of voxels. Third, their score is the expectation over several random initializations  $x_0$  while we only consider a single deterministic initialization, *i.e.*,  $x_0 = 0$ . We consider this adaptation reasonable since it initializes with a feasible point, and we optimize a convex function instead of a highly non-convex one, as is usual in deep learning.

### 4.1. Related work

Paul et al. (2021) were not the first to consider gradient norms as measures of informativeness in neural network training, as similar ideas were already leveraged by, *e.g.*, Alain et al. (2016) and Katharopoulos and Fleuret (2018).

Regarding radiation treatment planning, several performance-improving approaches have been proposed. Thieke et al. (2002) sample pencil beams with a probability based on the radial distance between its central ray and a particular voxel. They are able to reduce the dose-influence matrix to a third of its original size without impacting the quality of the resulting treatment plan. Yang and Xing (2004) use an iterative algorithm to solve a weighted least squares problem, where each voxel’s weight is updated based on the current dose of that voxel. For a target voxel, the weight is negatively correlated with the dose, while for an OAR voxel, the weight is positively correlated. The update equation depends on structure-specific parameters, which are found via trial and error. Zakarian and Deasy (2004) review several strategies for increasing the speed and efficiency of dose calculations, including a method based on fast wavelet transforms. Scherrer et al. (2005) employ adaptive hierarchical clustering to reduce the size of the treatment planning problem. Starting with a coarse clustering of voxels, they replace each cluster with the mean of its component voxels, solve the optimization problem using the mean data, and locally refine the clusters based on this solution. The process continues until the solution is sufficiently close to that of the original problem, based on a derived error bound. Numerical experiments showed that their adaptive clustering reduced the computation time substantially. Martin et al. (2007) formulate the treatment planning problem as an optimization problem with a sum of separable objectives. To solve it, they employ stochastic steepest descent with voxel sampling in each iteration. The authors compare the results from uniform sampling, manual sampling of each structure, and objective-specific sampling rates chosen by minimizing the variance of the total estimated objective. They find that the objective-specific rates provide the largest speed improvement compared to regular steepest descent. Sjölund et al. (2019) perform sector-duration optimization for stereotactic radiosurgery by solving a linear programming problem. As this problem is large, they reduce the solution time by uniformly sampling positions at random in each structure and solving the associated dual problem, resulting in time savings. Fu et al. (2019) tackle the treatment planning problem with dose-volume constraints. This problem is a computationally challenging mixed-integer program. To arrive at a solution, they first solve a convex approximation of the problem, then use the result to select a subset of voxels to dose bound so the dose-volume constraints are met with the smallest margin. Ungun et al. (2019) solve a compressed approximation of the treatment planning problem by clustering voxels and beams with  $k$ -means clustering. Using duality theory, they bound the optimality gap between the approximate and true solution. With the proper choice of clusters, they are able to attain a substantial speedup while still producing an excellent treatment plan.

## 5. Conclusion

In this paper, we introduced the idea of subsampling large sets of voxels via importance sampling. We derived a sampling distribution based on a score that reflects the

*informativeness* of a voxel. This score was derived by first pre-solving a simplified optimization problem and then using the gradient norm to measure a voxel’s importance. Using this subsampling technique allows us to significantly reduce the number of voxels, thus obtaining a much smaller optimization problem, which we can solve much faster. Empirical evaluations on three openly available cases showcase the efficacy of our proposed approach. For example, on a prostate case, using only 7.5% of voxels yields deviations of the objective function on all voxels of less than 1% while only taking less than 7% of the time to compute. In summary, our approach has the potential to significantly accelerate planning times while maintaining the plan quality.

## Acknowledgments

This work was partially supported by the Wallenberg AI, Autonomous Systems and Software Program (WASP) funded by the Knut and Alice Wallenberg Foundation; as well as Sweden’s Innovation Agency (Vinnova) project 2022-03023.

## Data availability statement

We use the publicly available CORT data set from Craft et al. (2014).


## Conflicts of interest


The authors declare no conflict of interest.


## Author contributions

**Sebastian Mair:** Conceptualization, Formal Analysis, Investigation, Methodology, Software, Visualization, Writing - Original Draft. **Anqi Fu:** Validation, Writing - Review and Editing. **Jens Sjölund:** Conceptualization, Funding Acquisition, Project Administration, Validation, Writing - Review and Editing.

## ORCID iDs

Sebastian Mair  <https://orcid.org/0000-0003-2949-8781>

Anqi Fu  <https://orcid.org/0000-0002-2876-2942>

Jens Sjölund  <https://orcid.org/0000-0002-9099-3522>

## Appendix A. Deriving the importance score

To derive importance scores, we adapt an approach from Paul et al. (2021) to our scenario. The idea is as follows. We start by optimizing a cheap surrogate optimization problem, *i.e.*, the probing function in Equation (4). Let  $\tilde{f}_s(y_v) \stackrel{\text{def}}{=} \frac{1}{|V_s|} f_s(y_v)$  and

$g_k(v) = \frac{d}{dx} \tilde{f}_s(y_v)$  denote the gradient of the probing function of voxel  $v$  at iteration  $k$  of projected gradient descent. For the sake of the argument, assume that the training dynamics are in continuous time instead of discrete iterations. The time derivative of the probing penalty for an arbitrary voxel  $v$  given the set of all voxels  $\mathcal{V}$  is

$$\Delta_k(v, \mathcal{V}) \stackrel{\text{def}}{=} -\frac{d\tilde{f}_s(y_v)}{dk} = -\frac{d\tilde{f}_s(y_v)}{dx_k} \frac{dx_k}{dk} = -g_k(v) \frac{dx_k}{dk},$$

where we first use the chain rule and then the definition of the function  $g_k(v)$ . Note that because of

$$\frac{dx_k}{dk} \approx x_{k+1} - x_k = -\eta \sum_{v \in \mathcal{V}} g_k(v),$$

we can simplify  $\Delta$  to

$$\Delta_k(v, \mathcal{V}) = \eta g_k(v) \sum_{v \in \mathcal{V}} g_k(v).$$

Adapting an argument from Paul et al. (2021), we can bound the contribution of an arbitrary voxel  $v$  as follows. Let  $\mathcal{V}_{-j}$  be the set of all voxels except the  $j$ th one. Then, for any voxel  $v$  the influence of having the  $j$ th voxel included during training can be bounded via

$$\begin{aligned} \|\Delta_k(v, \mathcal{V}) - \Delta_k(v, \mathcal{V}_{-j})\| &= \left\| \eta g(v) \sum_{v \in \mathcal{V}} g_k(v) - \eta g(v) \sum_{v \in \mathcal{V}_{-j}} g_k(v) \right\| \\ &= \|\eta g(v) g_k(v = j)\| \leq \|\eta g(v)\| \cdot \|g_k(v = j)\|. \end{aligned}$$

Since  $\|\eta g(v)\|$  is a constant for all  $j$ , it can be neglected. Thus, the influence of a voxel  $v$  given the current beam intensities  $x_k$  during optimization depends on its gradient norm. Phrased differently, voxels with a small gradient norm have a small influence on the overall per-voxel penalty. Likewise, we expect a high influence of voxels that have a large gradient norm. Hence, we define the importance score as  $\chi_k(v) = \|g_k(v)\|$ .

## Appendix B. Further results

First, Figure B1 depicts the same as Figure 1 but for the liver and head and neck cases. We can clearly see that body voxels that lie in the beam corridor get a higher probability of being sampled than regular body voxels. In general, most of the probability mass is placed at OARs and around the PTV.

Second, Figure B2 visualizes the dose-volume histograms as dashed lines for the liver and head and neck cases after  $k = 20$  steps of projected gradient descent on Equation 4, which we use to derive our importance scores. Just as in Figure 3 (left), the dose-volume histograms derived from solving the full optimization problem of Equation (1) is depicted as solid lines for reference. As for the prostate case, the dose-volume histograms obtained from using the solutions  $x_{20}$  do not approximate the desired dose-volume histograms sufficiently well. However, as seen in Figure B1, the solutions  $x_{20}$  are sufficient to derive meaningful importance scores as seen by the sampling distributions.

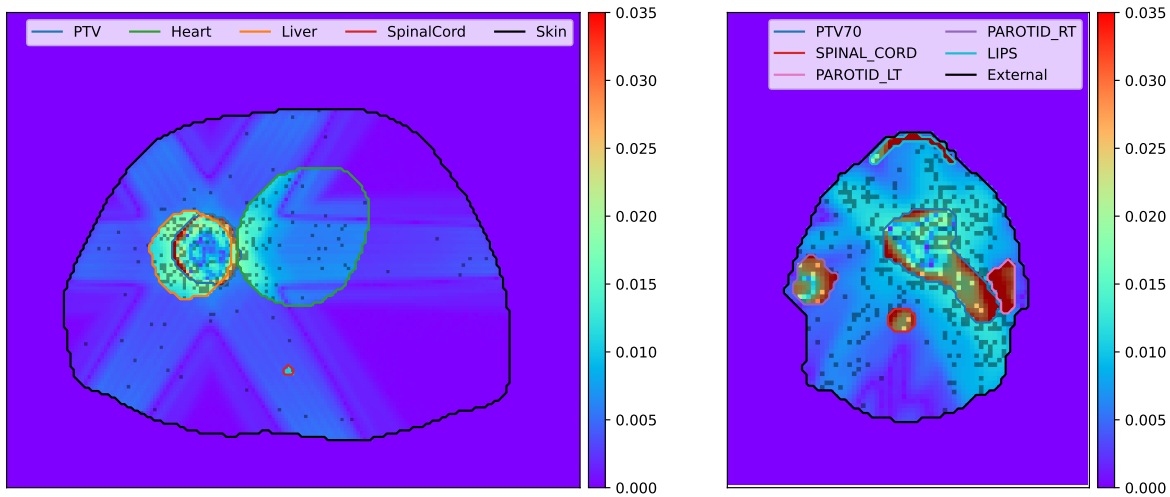


Figure B1: Sampling distribution  $q(v)$  for a liver (left) and head and neck case (right) including  $m = 9,637$  and  $m = 25,189$  sampled voxels corresponding to 0.5% and 10% of voxels, respectively.

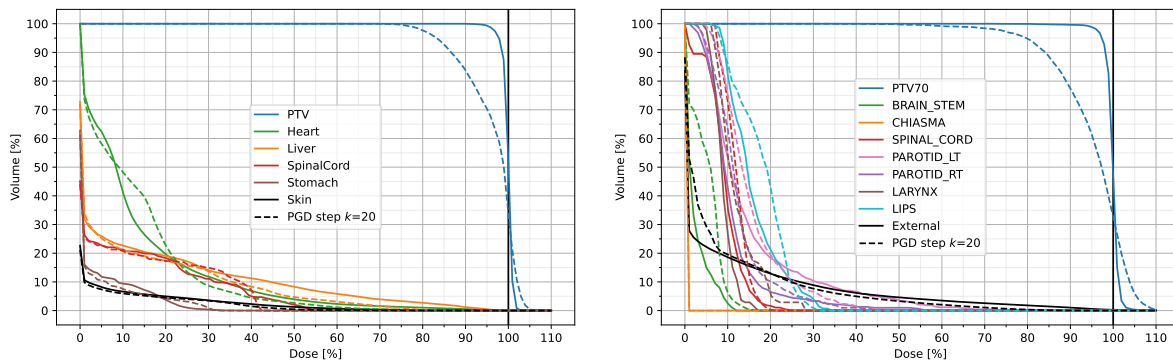


Figure B2: Dose-volume histograms for the liver (left) and the head and neck case (right) case of full (solid lines) and the projected gradient descent (PGD) optimization after  $k = 20$  steps (dashed lines) which we use as a probing function to derive the importance scores.

Next, Figures B3 and B4 show the same scenario as Figure 2 but for the liver and head and neck cases. The left columns show the performance of our proposed **gradnorm** score while the right columns depict the performance of a **uniform** subsample. Figure B3 shows that the liver case is especially easy to approximate using **gradnorm** and a very small subsample of just 0.1% of the total voxel amount. Contrary, **uniform** needs at least 25% to achieve a similar performance. The scenario is slightly different for the head and neck case as visualized in Figure B4 where as much as 10% of the voxels are needed to achieve an acceptable approximation.

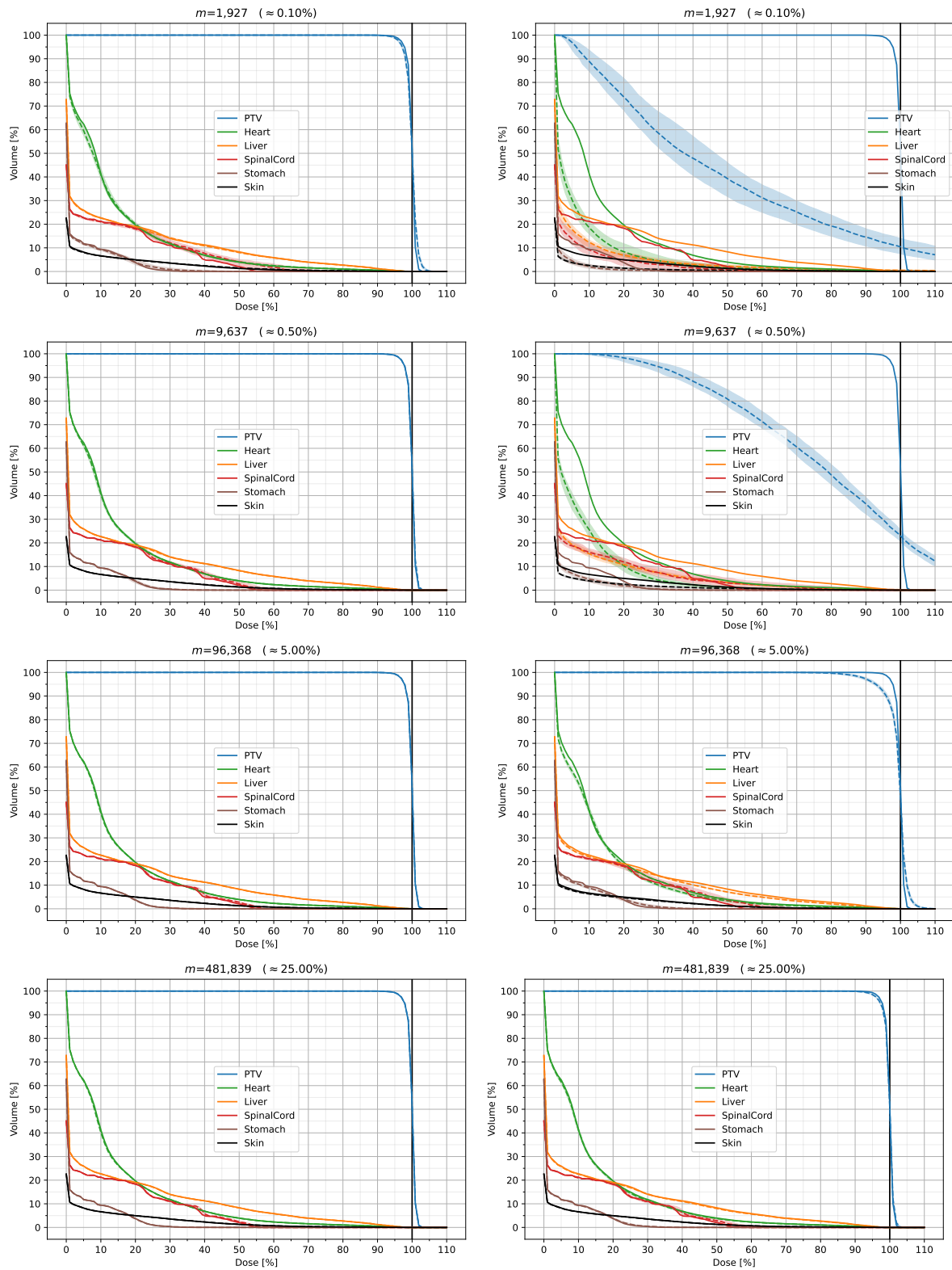


Figure B3: Dose-volume histograms for the liver case and  $p = 2$ . The left column depicts the results of our proposed `gradnorm` subsampling approach while the right column shows `uniform` subsampling. The rows depict different subsampling sizes  $m$ .

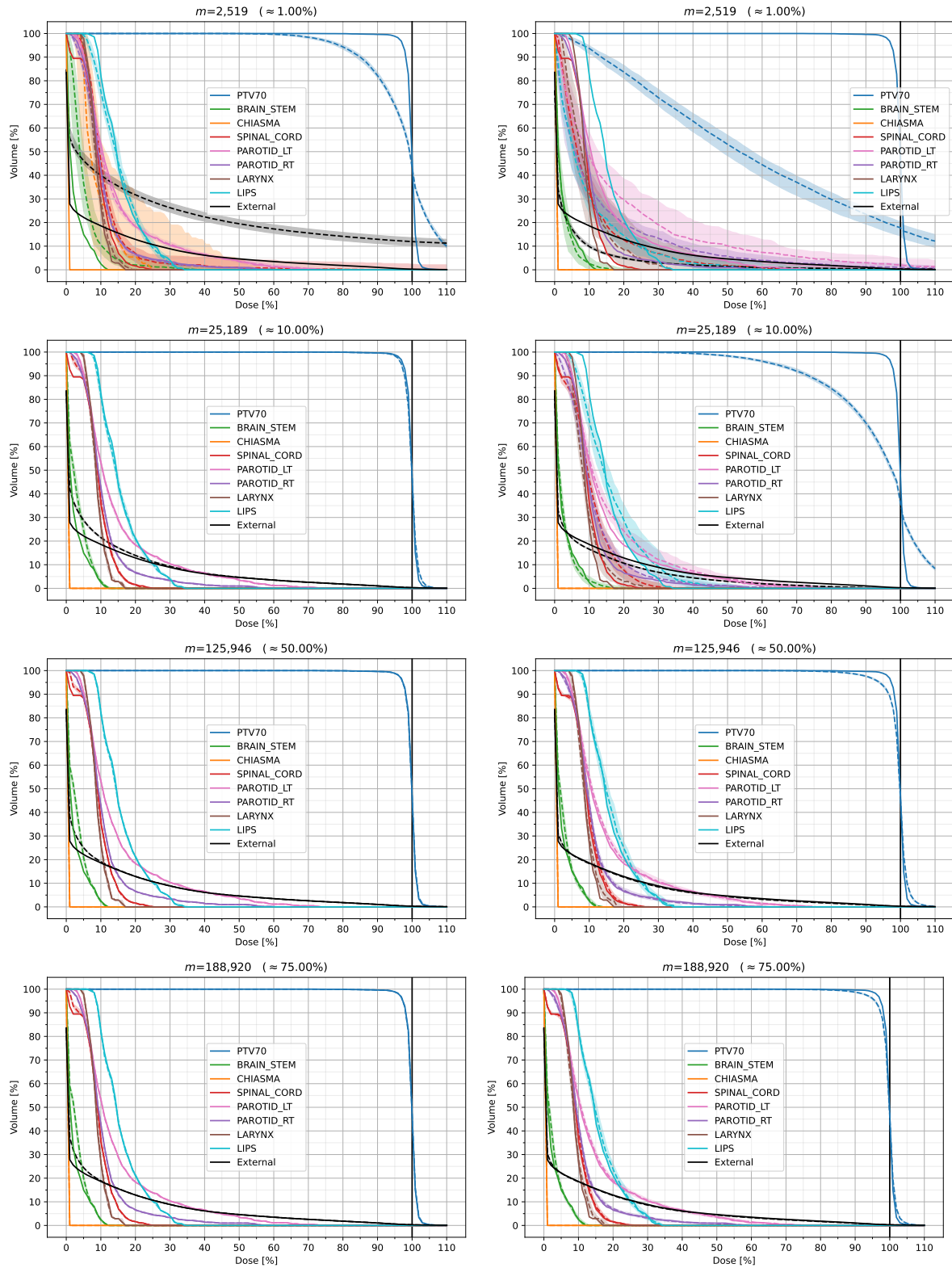


Figure B4: Dose-volume histograms for the head and neck case and  $p = 2$ . The left column depicts the results of our proposed gradnorm subsampling approach while the right column shows uniform subsampling. The rows depict different subsampling sizes  $m$ .



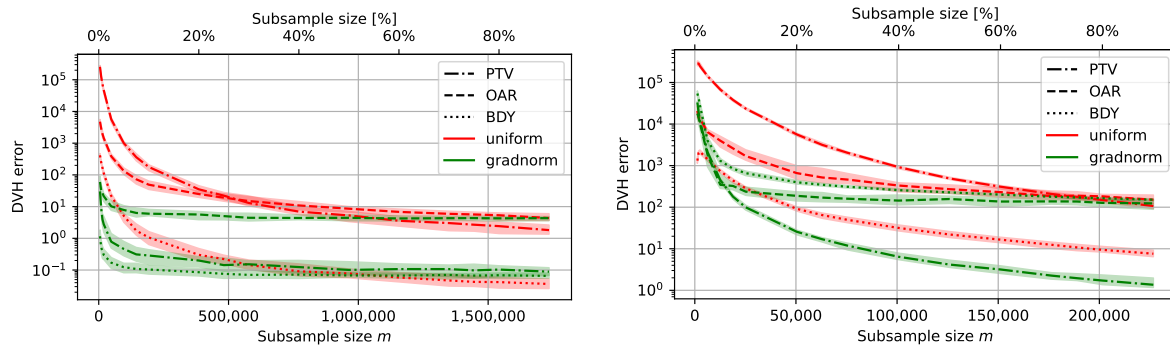


Figure B5: Error of dose-volume histogram approximations of **uniform** and **gradnorm** when compared to **full** for the liver (left) and the head and neck (right) case. The error is split among the structures  $S = \{PTV, OAR, BDY\}$ .

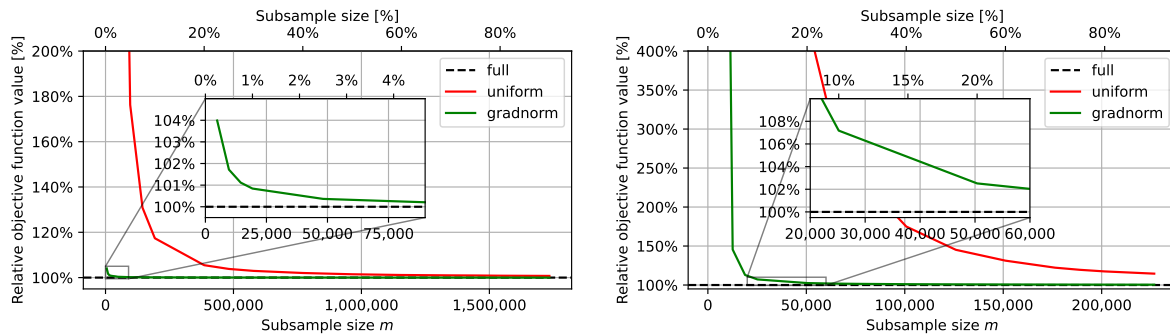


Figure B6: Relative objective function values of **uniform** and **gradnorm** when compared to **full** for the liver (left) and the head and neck (right) case.

Figure B5 depicts the error of dose-volume histogram approximations and we can see that the only structure on which **uniform** yields a better approximation than **gradnorm** is BDY. For the liver case, this is only true for large sample sizes but for the head and neck case, this effect is visible much earlier. This can be also seen in Figure B4 where the black line representing the BDY structure (named External) struggles to approximate the low dose region. However, we note that – in turn – the more important PTV and OAR structures are approximated sufficiently well.

The relative objective function approximations of **uniform** and **gradnorm** are shown in Figure B6 for the liver (left) and head and neck (right) case, respectively. For the liver case, **gradnorm** yields an error of less than 1% when using more than 1% of all voxels whereas **uniform** needs significantly more voxels to achieve a similar approximation. As mentioned above, the head and neck case appears to be more difficult and Figure B4 suggests that **gradnorm** needs at least 10% of the voxels. Now, Figure B6 (right) reveals that this choice yields an approximation of the objective function that only deviates 7% of the objective function value obtained from the **full** solution.

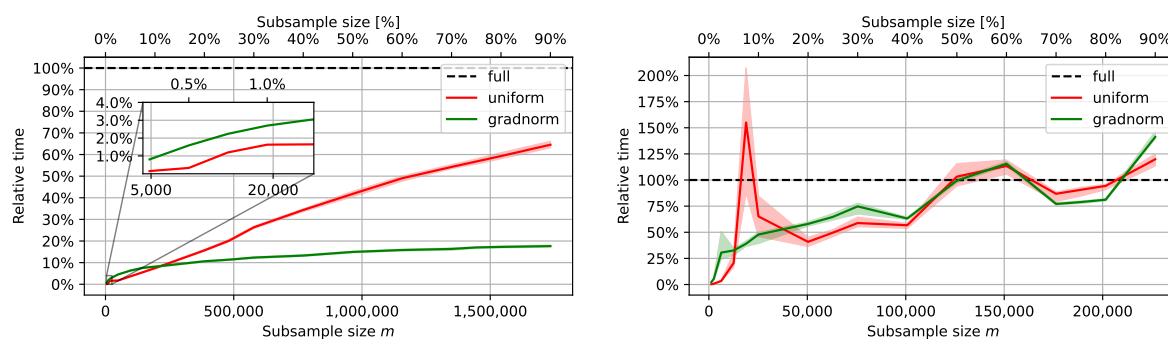


Figure B7: Computation time of **uniform** and **gradnorm** relative to **full** for the liver (left) and the head and neck (right) case.

Finally, Figure B7 depicts the relative computation times of solving the reduced optimization problems when compared to the time it takes to solve the corresponding full problem. For the liver case on the left-hand side, subsampling only 1% of all voxels using **gradnorm** lowers the computation times to less than 3% of the time **full** needs on all voxels. Whereas the optimization times are rather stable for the prostate and liver cases, the situation is – once again – different for the head and neck case. However, using the proposed 10% of all voxels using **gradnorm** allows us to reduce the computation time to less than 50%.

**References**

- Ahnesjö, A. and Aspradakis, M. M. (1999). Dose calculations for external photon beams in radiotherapy, *Physics in Medicine & Biology* **44**(11): R99.
- Alain, G., Lamb, A., Sankar, C., Courville, A. and Bengio, Y. (2016). Variance reduction in sgd by distributed importance sampling, *International Conference on Learning Representations - Workshop Track*.
- Aleman, D. M., Glaser, D., Romeijn, H. E. and Dempsey, J. F. (2010). Interior point algorithms: guaranteed optimality for fluence map optimization in IMRT, *Physics in Medicine & Biology* **55**(18): 5467.
- Craft, D., Bangert, M., Long, T., Papp, D. and Unkelbach, J. (2014). Shared data for intensity modulated radiation therapy (IMRT) optimization research: the CORT dataset, *GigaScience* **3**(1): 2047–217X.
- Diamond, S. and Boyd, S. (2016). CVXPY: a Python-embedded modeling language for convex optimization, *Journal of Machine Learning Research* **17**(83): 1–5.
- Fippel, M. (1999). Fast Monte Carlo dose calculation for photon beams based on the VMC electron algorithm, *Medical Physics* **26**(8): 1466–1475.
- Fu, A., Ungun, B., Xing, L. and Boyd, S. (2019). A convex optimization approach to radiation treatment planning with dose constraints, *Optimization and Engineering* **20**: 277–300.
- Harris, C. R., Millman, K. J., van der Walt, S. J., Gommers, R., Virtanen, P., Cournapeau, D., Wieser, E., Taylor, J., Berg, S., Smith, N. J., Kern, R., Picus, M., Hoyer, S., van Kerkwijk, M. H., Brett, M., Haldane, A., del Río, J. F., Wiebe, M., Peterson, P., Gérard-Marchant, P., Sheppard, K., Reddy, T., Weckesser, W., Abbasi, H., Gohlke, C. and Oliphant, T. E. (2020). Array programming with NumPy, *Nature* **585**(7825): 357–362.
- Katharopoulos, A. and Fleuret, F. (2018). Not all samples are created equal: Deep learning with importance sampling, *International Conference on Machine Learning*, PMLR, pp. 2525–2534.
- Martin, B. C., Bortfeld, T. R. and Castanon, D. A. (2007). Accelerating IMRT optimization by voxel sampling, *Physics in Medicine & Biology* **52**(24): 7211.
- Miettinen, K. (1999). *Nonlinear multiobjective optimization*, Vol. 12, Springer Science & Business Media.
- O’Donoghue, B., Chu, E., Parikh, N. and Boyd, S. (2016). Conic optimization via operator splitting and homogeneous self-dual embedding, *Journal of Optimization Theory and Applications* **169**(3): 1042–1068.
- Paul, M., Ganguli, S. and Dziugaite, G. K. (2021). Deep learning on a data diet: Finding important examples early in training, *Advances in Neural Information Processing Systems*, Vol. 34, pp. 20596–20607.

- Romeijn, H. E., Ahuja, R. K., Dempsey, J. F., Kumar, A. and Li, J. G. (2003). A novel linear programming approach to fluence map optimization for intensity modulated radiation therapy treatment planning, *Physics in Medicine & Biology* **48**(21): 3521.
- Romeijn, H. E., Dempsey, J. F. and Li, J. G. (2004). A unifying framework for multi-criteria fluence map optimization models, *Physics in Medicine & Biology* **49**(10): 1991.
- Scherrer, A., Küfer, K.-H., Bortfeld, T., Monz, M. and Alonso, F. (2005). Imrt planning on adaptive volume structures—a decisive reduction in computational complexity, *Physics in Medicine & Biology* **50**(9): 2033–2053.
- Sjölund, J., Riad, S., Hennix, M. and Nordström, H. (2019). A linear programming approach to inverse planning in Gamma Knife radiosurgery, *Medical Physics* **46**(4): 1533–1544.
- Stellato, B., Banjac, G., Goulart, P., Bemporad, A. and Boyd, S. (2020). OSQP: an operator splitting solver for quadratic programs, *Mathematical Programming Computation* **12**(4): 637–672.
- Thieke, C., Nill, S., Oelfke, U. and Bortfeld, T. (2002). Acceleration of intensity-modulated radiotherapy dose calculation by importance sampling of the calculation matrices, *Medical Physics* **29**(5): 676–681.
- Ungun, B., Xing, L. and Boyd, S. (2019). Real-time radiation treatment planning with optimality guarantees via cluster and bound methods, *INFORMS Journal on Computing* **31**(3): 544–558.
- Unkelbach, J., Bortfeld, T., Craft, D., Alber, M., Bangert, M., Bokrantz, R., Chen, D., Li, R., Xing, L., Men, C. et al. (2015). Optimization approaches to volumetric modulated arc therapy planning, *Medical Physics* **42**(3): 1367–1377.
- Wächter, A. and Biegler, L. T. (2006). On the implementation of an interior-point filter line-search algorithm for large-scale nonlinear programming, *Mathematical Programming* **106**: 25–57.
- Yang, Y. and Xing, L. (2004). Inverse treatment planning with adaptively evolving voxel-dependent penalty scheme, *Medical Physics* **31**(10): 2839–2844.
- Zakarian, C. and Deasy, J. (2004). Beamlet dose distribution compression and reconstruction using wavelets for intensity modulated treatment planning, *Medical Physics* **31**(2): 368–375.